



HAL
open science

High-Nb alkaline mafic dykes in the central Alps witness to the Triassic evolution of the Adria passive margin

Marco Filippi, Davide Zanoni, Massimo Tiepolo, Michel Corsini, Gisella Rebay, Jean-Marc Lardeaux, Maria Iole Spalla

► To cite this version:

Marco Filippi, Davide Zanoni, Massimo Tiepolo, Michel Corsini, Gisella Rebay, et al.. High-Nb alkaline mafic dykes in the central Alps witness to the Triassic evolution of the Adria passive margin. *Lithos*, 2023, 464-465, 10.1016/j.lithos.2023.107435 . hal-04368725

HAL Id: hal-04368725

<https://hal.science/hal-04368725>

Submitted on 1 Jan 2024

HAL is a multi-disciplinary open access archive for the deposit and dissemination of scientific research documents, whether they are published or not. The documents may come from teaching and research institutions in France or abroad, or from public or private research centers.

L'archive ouverte pluridisciplinaire **HAL**, est destinée au dépôt et à la diffusion de documents scientifiques de niveau recherche, publiés ou non, émanant des établissements d'enseignement et de recherche français ou étrangers, des laboratoires publics ou privés.



High-Nb alkaline mafic dykes in the central Alps witness to the Triassic evolution of the Adria passive margin

Marco Filippi^{a,b,*}, Davide Zanoni^a, Massimo Tiepolo^a, Michel Corsini^b, Gisella Rebay^c, Jean-Marc Lardeaux^{b,d}, Maria Iole Spalla^a

^a Dipartimento di Scienze della Terra “A. Desio”, Università degli Studi di Milano, Via Mangiagalli 34, 20133 Milano, Italy

^b UMR Géozur, Université Côte d’Azur, Observatoire de la Côte d’Azur, CNRS, IRD, 250 Rue A. Einstein, Sophia-Antipolis, 06560 Valbonne, France

^c Dipartimento di Scienze della Terra e dell’Ambiente, Università degli Studi di Pavia, Via Ferrata 1, 27100 Pavia, Italy

^d Centre for Lithospheric Research, Czech Geological Survey, Klárov 3, 118 21 Prague 1, Czech Republic

ARTICLE INFO

Keywords:

Southalpine domain
Lithospheric thinning
Pangea break-up
Syn-rift magmatism
Biotite ⁴⁰Ar / ³⁹Ar dating

ABSTRACT

The Edolo diabase dykes intruded the Variscan basement in the central Southalpine domain. Biotite ⁴⁰Ar / ³⁹Ar dating shows that the emplacement occurred during the final stage of Permian-Triassic lithospheric thinning. In this phase on the Adria passive margin, middle Triassic magmatism with disputed arc affinity is followed by a late Triassic alkaline event associated with continental rifting. The Edolo diabase dykes are Ti-rich and alkaline, with high Nb and Ta contents and ratios in igneous amphibole, biotite, and ilmenite. These features are typical of the late Triassic magmatism. In contrast, the early-crystallized clinopyroxene shows low Nb and Ta contents and ratios and an apparent arc affinity may be thus envisaged in the clinopyroxene parental melt. However, given the coexistence of both features in the same dykes, their composition cannot be interpreted in terms of transition between tectonic environments. Instead, it is likely attributed to the heterogeneity of the Adriatic lithosphere inherited from the Variscan to Permian evolution, which underwent asthenospheric upwelling due to Permian-Triassic extensional tectonics.

1. Introduction

The Permian-Triassic period in the Alpine domains is characterized by extension and lithospheric thinning, which led HT (high-temperature) metamorphism in the basement rocks and mantle-derived magmatism (Lardeaux and Spalla, 1991; Rebay and Spalla, 2001; Roda et al., 2019, 2023; Schuster and Stüwe, 2008; Spalla et al., 2014). The extensional tectonics has persisted continuously for a hundred million years leading to the Jurassic oceanization (Marotta et al., 2018; Roda et al., 2019), despite the volcano-sedimentary basins display diachronous stages of subsidence and exhumation (Berra and Carminati, 2010) and the volumes of emplaced mafic igneous rocks decrease over time.

In the western Alps, Permian metamorphism is extensively recorded in the Austroalpine and Southalpine domains (Lardeaux and Spalla, 1991; Manzotti et al., 2018; Rebay and Spalla, 2001) and, in the latter, the thermal perturbation also characterized the Triassic evolution (Guergouz et al., 2018; Klötzli et al., 2014; Peressini et al., 2007; Smye et al., 2019). In apparent contrast, a substantial portion of the Variscan basement in Southalpine domain of central and eastern Alps escaped the

Permian-Triassic HT metamorphism because it had already been exhumed at the end of the Variscan evolution (Spalla et al., 2009; Zanoni et al., 2010; Zanoni and Spalla, 2018; Filippi et al., 2021 and ref. therein), with the exception of the Triassic Dervio Olgiasca unit (Fig. 1, Diella et al., 1992; Bertotti et al., 1993; di Paola and Spalla, 2000; Spalla et al., 2000; Real et al., 2023). In these crustal levels, lithospheric thinning is evidenced by transtensional to extensional faulting accommodating the deposition of Carboniferous to Mesozoic sedimentary covers (De Graciansky et al., 2011; Zanchi et al., 2019) and Permian-Triassic volcanoclastites and dykes (Beltrán-Triviño et al., 2016; Berra et al., 2015; Cassinis et al., 2008; Schaltegger and Brack, 2007; Storck et al., 2019). Xenoliths of Permian granulites within Oligocene trachytes (Sassi et al., 2020) are indirect evidence of HT Permian-Triassic metamorphism in the eastern Southalpine domain.

The Permian-Triassic HT metamorphism is coeval with mafic magma emplacements at various depths along the Adria passive margin and these rocks exhibit a consistent compositional evolution over time. After the emplacement of voluminous tholeiitic gabbros in the Permian, the scattered middle Triassic magmatism shifted from calc-alkaline to

* Corresponding author at: Dipartimento di Scienze della Terra “A. Desio”, Università degli Studi di Milano, Via Mangiagalli 34, 20133 Milano, Italy.
E-mail address: marco.filippi@unimi.it (M. Filippi).

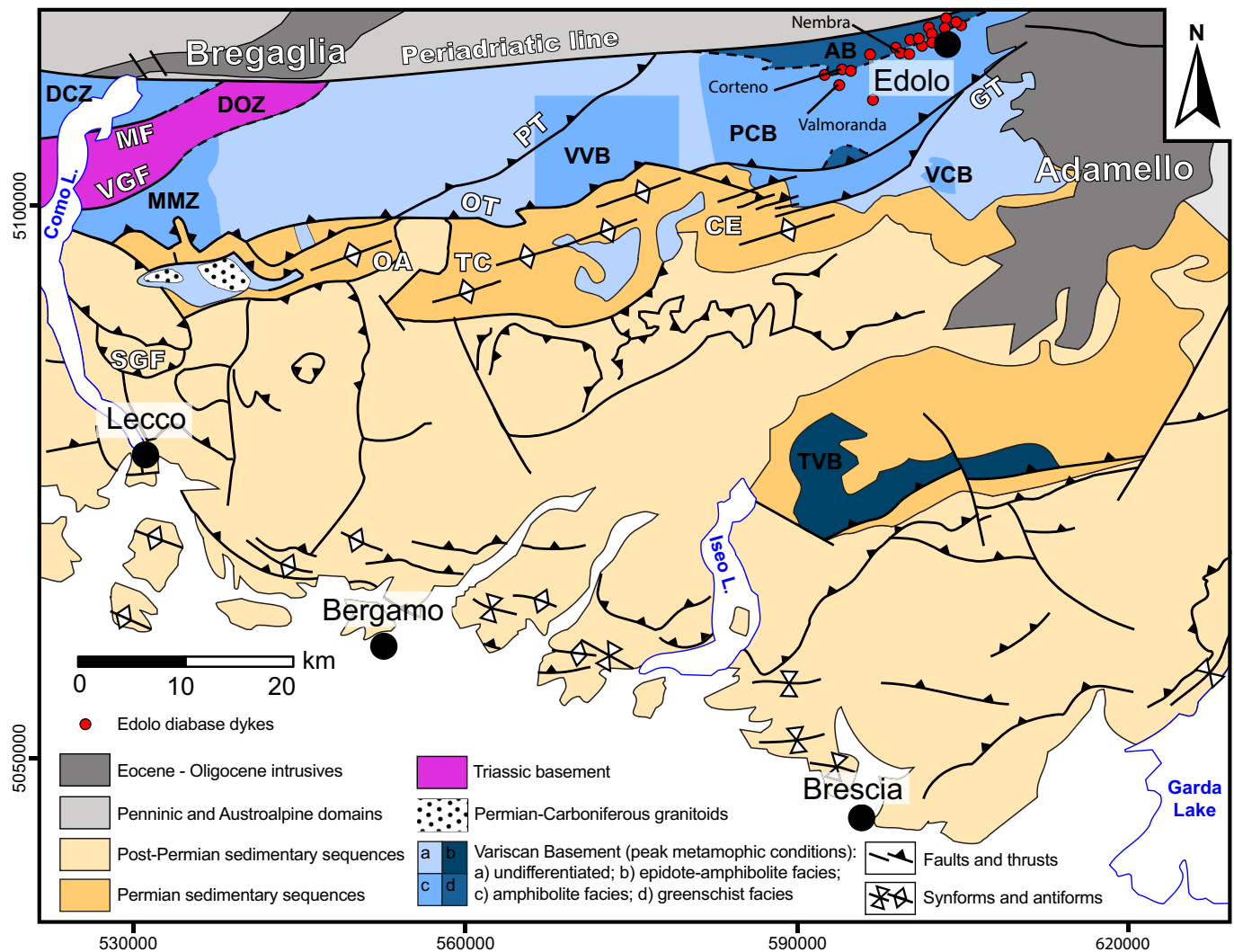


Fig. 1. Geologic sketch of the central Southalpine domain with location of the Edolo diabase dykes (modified after Filippi et al., 2022, and refs therein). Variscan tectono-metamorphic units: AB = Aprica basement; DCZ = Domaso – Cortafo Zone; DOZ = Dervio – Olgiasca Zone; MMZ = Monte Muggio Zone; PCB = Passo Cavalcafciche Basement; TVB = Tre Valli Bresciane Basement; VCB = Upper Val Camonica Basement; VVB = Val Vedello Basement. Regional scale structures: CE = Cedegolo anticline; GT = Gallinera thrust; MF = Musso fault; OA = Orobic anticline; OT = Orobic thrust; PT = Porcile thrust; SGF = Southern Grigna fault; TC = Trabucchetto-Cabianca anticline; VGF = Val Grande fault. Coordinate system: WGS84-UTM32N.

shoshonitic, later transitioning to alkaline and carbonatitic in the late Triassic (Casetta et al., 2018a, 2018b, 2019; De Min et al., 2020; Denyszyn et al., 2018; Lustrino et al., 2019; Quick et al., 2009; Sloman, 1989; Storck et al., 2019; Tribuzio et al., 1999).

In this study, we present a field, petrological, geochemical, and geochronological study of the Edolo diabase, which consists of a swarm of mafic dykes emplaced into the Variscan basement in the central Southalpine domain and intersecting the sequence of *syn*-metamorphic Variscan structures. This study aims to enhance the record of the Permian-Triassic magmatism along the Adria passive margin and to compare the features of the Edolo diabase dykes with those of coeval magmatic rocks in other portions of the Southalpine domain.

2. Geological setting

The metamorphic basement of the central Southalpine domain retains contrasting Variscan P-T (pressure – temperature) evolutions allowing for contouring of tectono-metamorphic units. Among them, the Passo Calvalcafciche, Domaso-Cortafo, and Tre Valli Bresciane Massif units (Fig. 1) retain the effects of superposed thermal states compatible with early Variscan burial and collision (Spalla et al., 1999; di Paola

et al., 2001 and ref. therein), whereas the Val Vedello, Monte Muggio, and Aprica units (Fig. 1) only record the Barrovian metamorphic imprint of the Variscan collision (Diella et al., 1992; Gosso et al., 1997). These tectono-metamorphic units were already exposed at surface in Permian times, according to the metamorphic evolution recorded in the clasts of the lower Permian sequences capping the Variscan basement and intersecting all the Variscan structures (Spalla et al., 2009; Zanoni et al., 2010; Zanoni and Spalla, 2018). Syn-exhumation heating is recorded in the upper Camonica valley basement prior to the late Permian (Filippi et al., 2021), and in the Dervio-Olgiasca unit in the Triassic (Fig. 1, Diella et al., 1992; di Paola and Spalla, 2000; Spalla et al., 2000; Real et al., 2023).

The Edolo diabase dykes intruded the Aprica and Passo Cavalcafciche units in the northern part of the central Southalpine, in between the Alpine Gallinera and Periadriatic lines (Fig. 1). These units mostly consist of metapelites and quartzites, in part derived from Ordovician-Silurian sediments, with minor lenses of orthogneiss (Gosso et al., 2012).

The dominant structure in the Aprica and Passo Cavalcafciche units is the Variscan S2 foliation that developed during the tectonic coupling of these units. This foliation is supported by greenschist facies minerals (Qz + Wm + Chl + Ab + Ttn) and dips 30–80° towards NNW (Rebay

et al., 2015). S2 developed under perturbed thermal conditions in both the units (Passo Cavalcafciche: $T < 400\text{--}550\text{ }^{\circ}\text{C}$, $P < 0.3\text{--}0.4\text{ GPa}$; Aprica: $T < 300\text{--}350\text{ }^{\circ}\text{C}$, $P < 0.3\text{ GPa}$), which are compatible with a late orogenic evolution (Gosso et al., 2012; Rebay et al., 2015; Spalla et al., 1999; Zanon et al., 2010).

The northern part of the central Southalpine domain displays heterogeneous deformation effects resulting from Alpine convergence. In the high strain domains, the Alpine convergence is testified by chevron folds coupled with south-verging thrusts, which also affect Permian and Mesozoic sedimentary sequences (Carminati et al., 1997; Rebay et al., 2015 and ref. therein). The Alpine folds are characterized by sub-horizontal NE – SW trending axes and axial planes steeply dipping towards NW or SE, alongside a locally developed S3 axial plane foliation.

The Edolo diabase dykes have been extensively mapped within the Passo Cavalcafciche and Aprica units where they intersect the Variscan S2 foliation (Filippi et al., 2022; Rebay et al., 2015; Schiavinato, 1954). Based on the intersection relations a possible Triassic age of intrusion was suggested in the past (Schiavinato, 1954). The dykes are sub-vertical and W-SW striking. Locally, igneous minerals are pervasively affected by static overgrowth of lower greenschist facies minerals, which developed during late intrusive fluid circulation at temperature of $300\text{--}350\text{ }^{\circ}\text{C}$ and pressure of $0.1\text{--}0.2\text{ GPa}$ (Filippi et al., 2022). The Alpine S3 foliation is locally developed along the margins of the dykes and is supported by greenschist facies minerals formed at a temperature of $350\text{--}420\text{ }^{\circ}\text{C}$ and a pressure of about 0.2 GPa (Filippi et al., 2022; Rebay et al., 2015). The samples for this study were carefully chosen from the central parts of the dykes to avoid greenschist facies minerals and thus ensuring the best preservation of igneous minerals and textures.

2.1. Field relations and petrography

This study is focused on the three main sites, Nembra, Corteno, and Valmoranda (Fig. 1), where swarms of meter-thick dykes intruded into the Variscan metapelites and quartzites of the Aprica and Passo Cavalcafciche units (Figs. 1, 2). The dykes are composed of clinopyroxene (20–25%), amphibole (10–15%), biotite (5–10%), plagioclase (45–50%), and ilmenite (5–10%), with accessory apatite. Exceptionally rare quartz and epidote grains are found in interstitial domains in the most differentiated samples. At the core, the dykes are hypidiomorphic with variable grain size. Locally, modally heterogeneous enclaves with lobate to blurred contacts are observed (Fig. 2). At the margins, the dykes are porphyritic to aphanitic (chilled margins), with clinopyroxene, amphibole, and plagioclase phenocrysts (Fig. 2). Leucocratic veins with gently lobate to straight margins are hosted within the dykes (Fig. 2). These veins are mostly composed of plagioclase (>90% vol) with minor amphibole and biotite.

3. Methods

Three samples from Nembra and four from Corteno (Table 1) were analyzed for WR (whole rock) major, trace, and rare earth elements at ActLabs (Canada) by ICP-OES (Inductively Coupled Plasma – Optical Emission Spectroscopy) and ICP-MS (Inductively Coupled Plasma – Mass Spectrometry). In addition, seven auxiliary samples from Valmoranda (Supplementary File S1) have been analyzed for major and trace elements at Università degli Studi di Genova by XRF (X-Ray Fluorescence).

Minerals from Nembra, Corteno, and Valmoranda dykes were analyzed at Università degli Studi di Milano with a JEOL 8200 Super

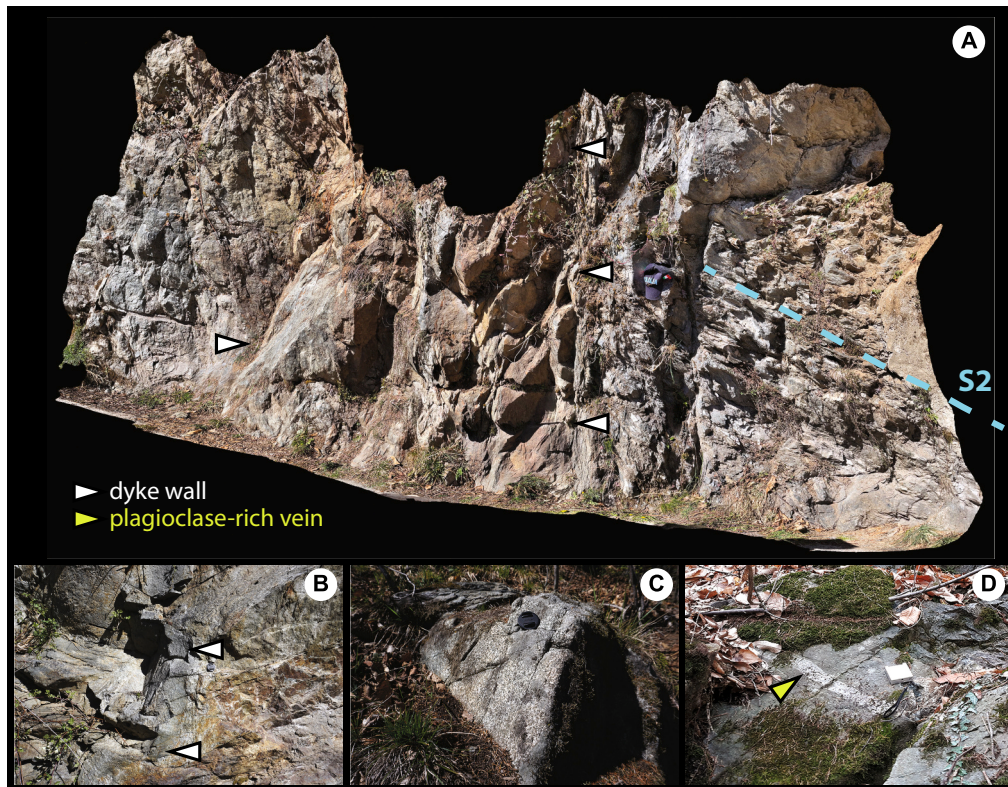


Fig. 2. Structural relationships and texture of Edolo diabase dykes. A: a metric-thick dyke intersecting the late-Variscan S2 foliation in metapelites in Nembra; hat for scale. B: detail on the chilled margin and pervasive hydrothermal alteration (yellow to brown) zone along a dyke wall in Corteno; camera cap for scale. C: plagioclase- and clinopyroxene-rich enclaves in a dyke in Nembra; camera cap for scale. D: a plagioclase-rich vein in a dyke in Nembra; compass for scale. (For interpretation of the references to colour in this figure legend, the reader is referred to the web version of this article.)

Table 1
WR composition (major, trace, and REE elements) of the Edolo diabase dykes.

Locality	Mafic dykes						
	Corteno	Corteno	Corteno	Corteno	Nembra	Nembra	Nembra
Sample	D34a	D34b	D32	Ge3	Ge10	Ge15	Ge16
SiO ₂ (wt%)	47.63	44.65	47.05	48.10	48.57	44.87	52.53
TiO ₂	3.41	2.75	2.11	2.33	2.61	3.08	2.06
Al ₂ O ₃	13.47	12.20	14.07	13.46	13.98	14.68	16.33
Fe ₂ O ₃	15.47	17.74	14.78	14.88	13.08	14.91	10.67
MgO	5.12	9.05	8.40	8.07	7.20	5.77	3.71
MnO	0.21	0.20	0.19	0.22	0.17	0.21	0.14
CaO	8.41	8.61	6.70	5.28	6.97	7.94	5.34
Na ₂ O	3.89	2.00	3.10	3.16	3.77	3.44	5.33
K ₂ O	1.06	1.48	0.85	1.32	1.56	1.85	1.25
P ₂ O ₅	0.62	0.22	0.33	0.34	0.56	1.13	0.73
LOI	1.00	1.72	2.88	3.26	2.23	1.75	2.16
Total	100.29	100.62	100.45	100.42	100.70	99.62	100.24
Mg#	0.39	0.50	0.52	0.51	0.52	0.43	0.40
Rb (ppm)	32	48	21	41	50	42	32
Ba	170	101	108	189	172	221	239
Th	3.1	1.5	2.5	2.1	3.8	3.8	5.6
U	0.9	0.5	0.7	0.7	1.2	1.1	1.6
Nb	25.2	17.9	23.1	25.5	44.6	50.1	57.5
Ta	1.3	0.96	1.22	1.32	2.25	2.53	2.81
Sr	390	222	263	264	499	579	515
Zr	155	107	140	141	196	213	265
Hf	4.4	3	3.7	3.8	5	4.8	6.6
Y	42.6	26.3	27.2	34.3	30.8	37.3	38.3
La	19	9.78	14.1	15.3	24.7	30.1	33.2
Ce	42.5	21.8	30.1	30.9	50.7	63	68.3
Pr	5.73	2.94	3.86	4.23	6.34	7.97	8.47
Nd	26.6	14.3	17.9	19.3	27.9	37.3	35.1
Sm	8.06	4.47	4.98	5.72	7.1	9.94	8.77
Eu	2.63	1.56	1.57	1.95	2.3	3.09	2.76
Gd	8.91	5.11	5.23	6.37	6.92	10	8.43
Tb	1.41	0.87	0.87	1.06	1.08	1.48	1.34
Dy	8.36	5.19	5.16	6.49	6.28	8.25	7.6
Ho	1.56	0.96	0.95	1.24	1.14	1.43	1.37
Er	4.13	2.56	2.62	3.38	3	3.67	3.62
Tm	0.521	0.341	0.35	0.452	0.379	0.448	0.479
Yb	3.1	2.07	2.1	2.75	2.22	2.61	2.84
Lu	0.478	0.317	0.323	0.421	0.339	0.387	0.417

Table 2
Compositional range (bold, apfu) and average value (\pm s.d., apfu) for clinopyroxene in the Edolo diabase dykes.

Locality	Rock type	Generation	Si	Ti	Al ^{VI}	Fe ²⁺	Fe ³⁺	Mg	Mg#	Ca	Na
Corteno	Mafic dyke	Cpx core	1.81–1.90	0.03–0.06	0.01–0.06	0.24–0.31	0.03–0.08	0.67–0.74	0.67–0.70	0.82–0.86	0.03–0.04
			1.85 \pm	0.05 \pm	0.03 \pm	0.27 \pm	0.06 \pm	0.71 \pm	0.69 \pm	0.84 \pm	
		(5 data)	0.03	0.01	0.02	0.02	0.02	0.03	0.01	0.01	–
		Cpx rim	1.98	0.01	0.04	0.28	0.00	0.71	0.72	0.94	0.02
		(1 data)	–	–	–	–	–	–	–	–	
Valmoranda	Mafic dyke	Cpx core	1.73–1.91	0.03–0.12	0.00–0.03	0.26–0.36	0.02–0.10	0.58–0.64	0.61–0.64	0.85–0.91	0.03–0.05
			1.80 \pm	0.08 \pm	0.02 \pm	0.31 \pm	0.06 \pm	0.62 \pm	0.63 \pm	0.87 \pm	0.04 \pm
		(10 data)	0.05	0.02	0.01	0.03	0.02	0.02	0.01	0.02	0.01
		Cpx rim	1.97–1.98	0.01–0.02	0.01–0.03	0.50–0.53	0.03–0.05	0.41–0.43	0.42–0.44	0.89–0.91	0.06–0.07
		(3 data)	–	–	0.01	0.01	0.01	0.01	0.01	–	
Nembra	Mafic dyke	Cpx core	1.75–1.92	0.03–0.08	0.02–0.06	0.18–0.31	0.00–0.09	0.66–0.78	0.66–0.76	0.83–0.87	0.03–0.05
			1.85 \pm	0.05 \pm	0.04 \pm	0.24 \pm	0.05 \pm	0.72 \pm	0.71 \pm	0.85 \pm	0.04 \pm
		(27 data)	0.05	0.01	0.01	0.03	0.02	0.04	0.03	0.01	0.01
		Cpx rim	1.87–1.99	0.00–0.04	0.00–0.05	0.30–0.46	0.00–0.09	0.52–0.74	0.52–0.71	0.84–0.94	0.01–0.05
		(10 data)	1.94 \pm	0.02 \pm	0.03 \pm	0.36 \pm	0.04 \pm	0.63 \pm	0.62 \pm	0.88 \pm	0.04 \pm
			0.04	0.01	0.02	0.06	0.03	0.07	0.06	0.03	0.01

Probe at 15 kV accelerating voltage and with a current beam of 5 nA. Natural silicates were used as standards. Amphibole formulae were calculated checking the most satisfying results of 13, 15, 16 cations and 23 oxygen normalizations following the methodology of [Locock \(2014\)](#). Oxo-components were considered only for nomenclature.

Clinopyroxene is recalculated at 4 cations and 6 O, feldspar at 4 O, and biotite at 11 O. The apatite formula is recalculated according to [Ketchum \(2015\)](#). Results of mineral-chemical analyses are shown in [Tables 2 and 3](#). The dataset is attached as Supplementary File S2.

Crystallization temperature (\pm 45 °C) and pressure (\pm 0.5 GPa) for

Table 3Compositional range (bold, apfu) and average value (\pm s.d., apfu) for magmatic amphibole in the Edolo diabase dykes.

Locality	Rock type	Generation	Si	Ti	Al ^{VI}	Mg#	Ca	Na	K	Cl	
Corteno	Mafic dyke	Amp core (3 data)	6.13–6.33 6.20 \pm 0.09	0.43–0.53 0.47 \pm 0.04	0.17–0.19 0.18 \pm 0.01	0.46–0.55 0.50 \pm 0.04	1.75–1.78 1.76 \pm 0.01	0.82–0.90 0.85 \pm 0.04	0.20–0.22 0.21 \pm 0.01	0.00–0.01 –	
		Amp rim (3 data)	6.08–6.27 6.15 \pm 0.09	0.25–0.40 0.31 \pm 0.06	0.19–0.34 0.28 \pm 0.06	0.22–0.27 0.25 \pm 0.02	1.73–1.83 1.79 \pm 0.05	0.77–1.00 0.86 \pm 0.10	0.27–0.31 0.29 \pm 0.02	0.00–0.01 –	
		Amp out. rim (4 data)	6.57–6.89 6.72 \pm 0.11	0.01–0.08 0.05 \pm 0.02	0.23–0.49 0.41 \pm 0.10	0.26–0.40 0.35 \pm 0.06	1.73–1.82 1.79 \pm 0.03	0.42–0.58 0.50 \pm 0.06	0.02–0.05 0.04 \pm 0.01	0.02–0.04 0.03 \pm 0.01	
		Plagioclase-rich vein	Amp core (2 data)	6.25–6.47 –	0.43–0.44 –	0.15–0.20 –	0.37 –	1.72–1.75 –	0.51–0.83 –	0.23 –	0.00–0.01 –
		Amp rim (4 data)	5.94–6.35 6.18 \pm 0.15	0.18–0.35 0.26 \pm 0.06	0.14–0.44 0.30 \pm 0.11	0.09–0.19 0.15 \pm 0.04	1.70–1.84 1.75 \pm 0.07	0.55–0.80 0.71 \pm 0.09	0.26–0.35 0.32 \pm 0.03	0.00–0.03 –	
		Amp out. rim (8 data)	6.06–6.66 6.29 \pm 0.19	0.04–0.12 0.07 \pm 0.03	0.16–0.66 0.46 \pm 0.16	0.16–0.29 0.20 \pm 0.05	1.80–1.90 1.86 \pm 0.03	0.39–0.87 0.63 \pm 0.14	0.05–0.22 0.11 \pm 0.06	0.10–0.24 0.13 \pm 0.05	
	Valmoranda	Mafic dyke	Amp core (2 data)	5.95–5.99 –	0.47–0.50 –	0.00–0.02 –	0.52–0.54 –	1.82–1.84 –	0.77–0.83 –	0.22 –	0.00 –
			Amp out. rim (1 data)	6.80 –	0.03 –	0.31 –	0.40 –	1.91 –	0.31 –	0.22 –	0.08 –
Nembra	Mafic dyke	Amp core (17 data)	6.04–6.34 6.18 \pm 0.08	0.45–0.64 0.53 \pm 0.05	0.16–0.32 0.21 \pm 0.04	0.44–0.56 0.50 \pm 0.04	1.74–1.85 1.79 \pm 0.02	0.40–0.93 0.76 \pm 0.13	0.18–0.26 0.23 \pm 0.02	0.00–0.03 0.01 \pm 0.01	
		Amp rim (13 data)	5.83–6.42 6.12 \pm 0.19	0.01–0.46 0.26 \pm 0.17	0.07–0.83 0.41 \pm 0.23	0.12–0.35 0.24 \pm 0.07	1.74–1.97 1.83 \pm 0.06	0.55–0.95 0.76 \pm 0.12	0.12–0.37 0.27 \pm 0.07	0.01–0.07 0.02 \pm 0.02	

igneous clinopyroxene was estimated by using the single-phase thermometer of Putirka (2008). Crystallization temperature (\pm 30 °C) for igneous amphibole was estimated applying the single-phase thermometer of Putirka (2016). Estimates on igneous amphibole crystallization pressure were avoided since amphibole barometers are less accurate than clinopyroxene barometers (see Putirka, 2016 for a discussion). Crystallization temperature for magmatic biotite (\pm 65 °C) is estimated by the single-phase thermometer of Li and Zhang (2022).

The concentrations of trace and REE elements in igneous clinopyroxene, amphibole, biotite, and ilmenite from Nembra and Corteno were determined at Università degli Studi di Milano by a Laser Ablation ICP-MS instrument consisting of a 193 nm ArF excimer laser equipped with a HelEx 2 volume sample chamber (Analyte Excite – Teledyne – Photon Machines) and a quadrupole ICP-MS (iCAP-Q Thermo Fisher Scientific). Ablation was performed with a spot diameter of 40 μ m, a frequency of 10 Hz, and a fluence of 2 J/cm². Each analysis included 40 s of background and 60 s of ablation signal acquisition. NIST612 glass was used as external standard in the analysis. Ca was used as internal standard for clinopyroxene and amphibole, Si for biotite, and Ti for ilmenite. BCR-2G glass was included in the analytical run as a quality control sample. The raw data was processed using GLITTER software (Van Achterbergh et al., 2001). The results are in Supplementary File S3.

Biotite ⁴⁰Ar/³⁹Ar geochronology was performed at Géoazur, Université Côte d'Azur with an ARGUS VI mass spectrometer from ThermoFischer. A sample from Nembra was crushed and a 300–500 μ m size fraction was cleaned in ultrasonic bath. Igneous biotite grains without evidence of alteration and inclusions were handpicked under a binocular microscope and packaged in aluminum foils and irradiated for 97 h in the McMaster Nuclear Reactor together with Fish Canyon sanidine grains as flux monitor (28.030 \pm 0.056 Ma, Jourdan and Renne, 2007). Raw data from each step and blank were processed, and ages were calculated using Ar – Ar CALC software (Koppers, 2002). The analytical procedure and raw data are in Supplementary File S4.

4. Results

4.1. WR geochemistry

The mafic dykes (Table 1, Supplementary Files S1) are alkaline basalts with SiO₂ at 44.5–52.5 wt%, Na₂O at 2.0–5.3 wt% and K₂O at 0.8–1.9 wt% (Fig. 3). The Mg# is between 0.4 and 0.6, with low LOI values at 1.0–3.3 wt%. MgO (3.7–10.7 wt%) shows a negative correlation with Cr (50–320 ppm, Fig. 3). The Ni content remains relatively

stable at around 140 ppm for MgO ranging from 5.1 to 10.7 wt%, and then decreases to 6–50 ppm in samples with the lowest MgO content (Fig. 3).

The chondrite-normalized incompatible element diagram (Fig. 3) reveals significant compositional variations among the localities. In Nembra, the profiles align closely with the reference OIB, but stand out for slightly higher Nb (45–58 ppm) and Ti contents, as well as Nb/Ta ratios. In contrast, the trace element concentrations in Corteno are significantly lower than in OIB (ocean island basalt). In addition, the mafic dykes in Corteno exhibit lower Nb contents (18–26 ppm) compared to those in Nembra, although their Ti contents and Nb/Ta ratios are similar. In comparison to the Triassic lamprophyres of the eastern Southalpine domain, the mafic dykes from Nembra and Corteno exhibit lower concentrations of Rb, Ba, and Sr, along with significantly higher Ti contents (Fig. 3).

The chondrite-normalized REE patterns show LREE enrichment over HREE, which are at about 10–20 times the CI chondrite without significant Eu anomalies (Fig. 3). Samples from Nembra display a higher LREE/HREE fractionation compared to those from Corteno, with (La/Yb)_N at 7.5–7.9 and 3.2–4.5, respectively. However, these values are lower than those of both OIB (11.6) and eastern Southalpine lamprophyres (5.6–10.4, Fig. 3).

4.2. Microstructure and mineral chemistry

4.2.1. Mafic dykes

Igneous clinopyroxene is pink at core and colorless at rim, with compositions grading from titanian diopside to diopside (Mg# = 0.6–0.7, Table 2). The clinopyroxene shows highly irregular grain boundaries and is locally rimmed by igneous amphibole and biotite (Fig. 4). The clinopyroxene cores are Na-poor and exhibit the highest Al and Ti contents (Fig. 5). In some cases, clinopyroxene is statically replaced by a late generation of green hornblende (Fig. 4).

Igneous amphibole is brown at core and pale brown to dark green at rim (Fig. 4). The core composition grades from ferri-kaersutite to Ti-rich pargasite (Mg# = 0.4–0.6, K = 0.2–0.3 apfu). The rim is ferro-pargasite (Mg# = 0.1–0.3), Ti-poorer and slightly K-richer than the core (Table 2, Fig. 5). Discontinuous and thin outer rims of blue-green amphibole are locally developed around the igneous amphibole (Fig. 4). The blue-green amphibole is ferro-ferri-hornblende (Mg# = 0.3–0.4, Table 3), characterized by the lowest Ti and K contents (Fig. 5).

Igneous biotite (annite, Mg# = 0.3–0.5) is dark brown and Ti-rich (Fig. 5), locally showing a pale brown to green rim (Fig. 4). Biotite

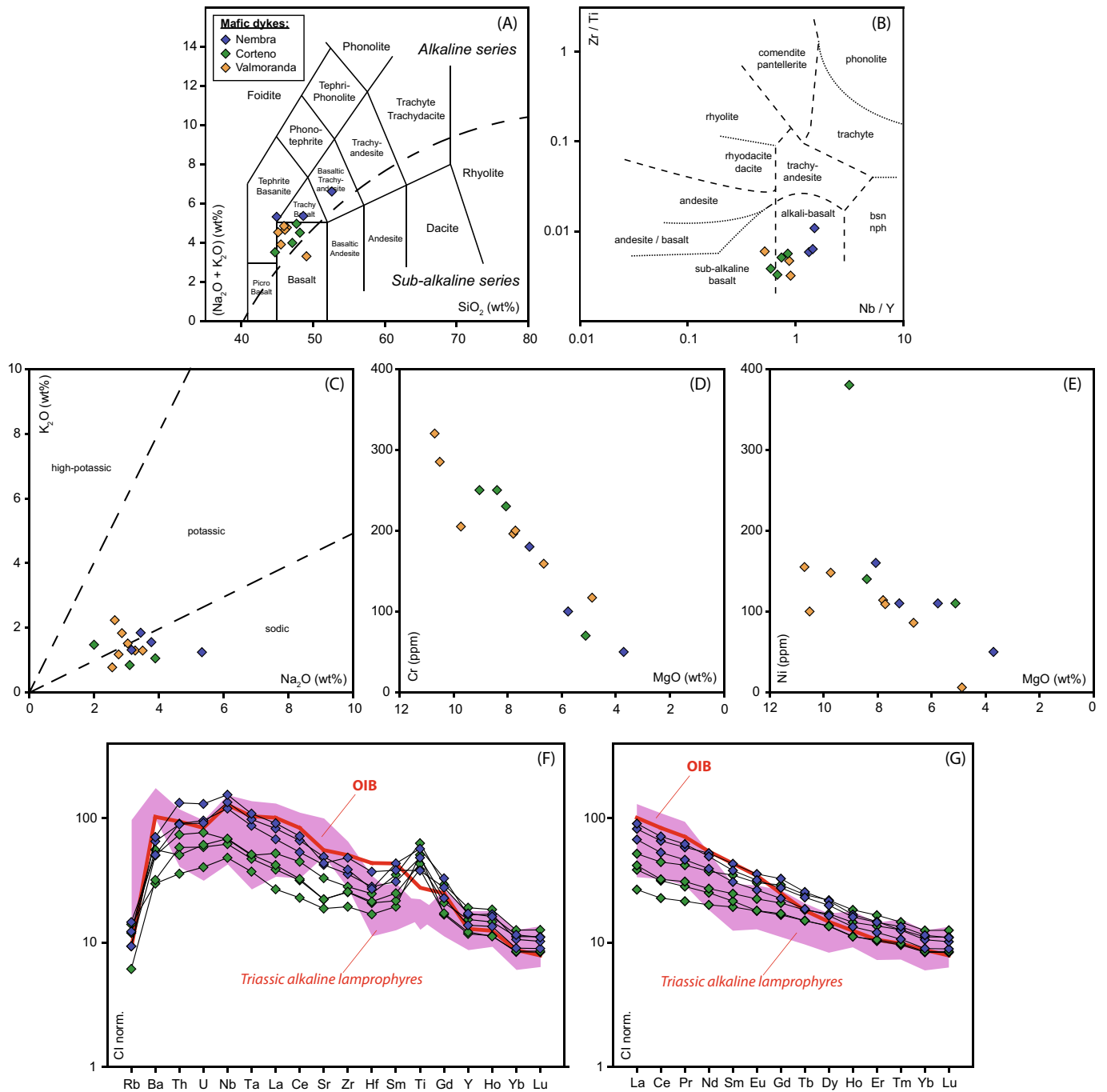


Fig. 3. WR compositions of the Edolo diabase dykes. A: Total Alkali versus Silica diagram. B: Nb/Y versus Zr/Ti classification diagram. C: K₂O vs Na₂O. D: Ni vs MgO. E: Cr vs MgO. F: chondrite-normalized incompatible element diagram. G: chondrite normalized REE diagram. The reference values for OIB (ocean island basalt) are from Sun and McDonough (1989). The compositions of Triassic alkaline lamprophyres from eastern Southalpine domain are from Casetta et al. (2019) and De Min et al. (2020).

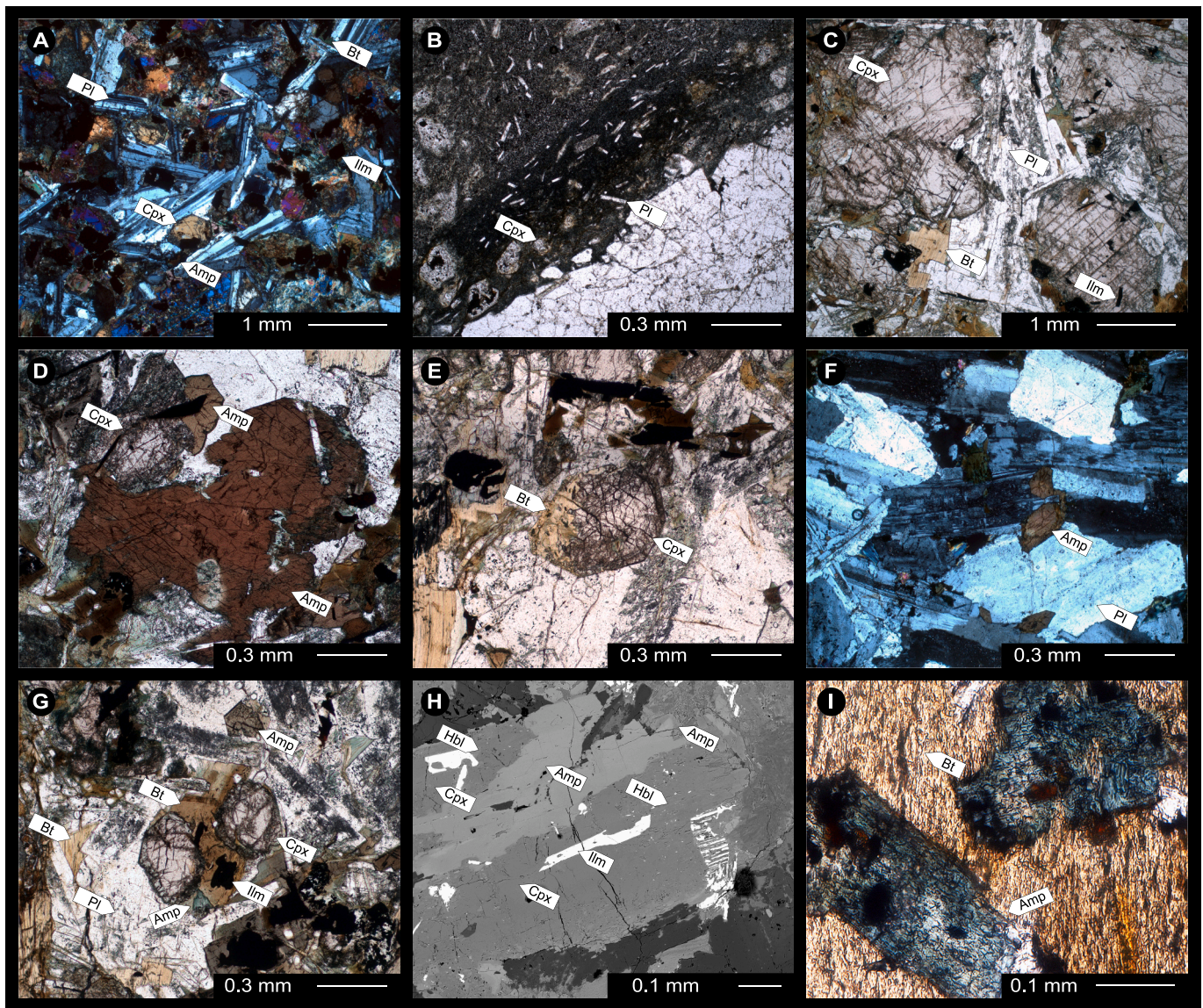


Fig. 4. Microphotographs of the Edolo diabase dykes (optical microscope and BSE imaging). A: hypidiomorphic texture characterized by euhedral to subhedral clinopyroxene and amphibole, along with subhedral to anhedral plagioclase and interstitial biotite, cross-polarized light. B: porphyritic texture with phenocrysts of plagioclase and clinopyroxene, plane-polarized light. C: clinopyroxene with plagioclase and interstitial biotite; plane-polarized light. D: igneous dark-brown amphibole surrounding a clinopyroxene grain with irregular boundaries, plane-polarized light. E: igneous biotite surrounding a clinopyroxene grain with irregular boundaries, plane-polarized light. F: plagioclase and amphibole in a plagioclase-rich vein; cross-polarized light. G: biotite and minor blue-green amphibole surrounding clinopyroxene grains with irregular boundaries, plane-polarized light. H: clinopyroxene partially replaced by hornblende and rimmed by igneous amphibole. An additional outer rim of blue-green amphibole is developed around this grain, in contact with hornblende, clinopyroxene, and igneous amphibole, BSE image. I: blue-green amphibole and biotite filling interstices between plagioclase, plane-polarized light. (For interpretation of the references to colour in this figure legend, the reader is referred to the web version of this article.)

rims clinopyroxene and fills interstitial domains between plagioclase grains (Fig. 4). Igneous plagioclase is euhedral to subhedral at cores (An_{48-63}) and displays simple and polysynthetic twins (Fig. 4). At rims, plagioclase (An_{6-24}) is untwinned and with lobate boundaries.

Ilmenite and apatite are commonly included in igneous clinopyroxene, biotite and amphibole (Fig. 4), together with very rare magnetite, rutile, and titanite in clinopyroxene. Apatite has intermediate composition between fluoroapatite and hydroxylapatite, according to significant F (0.83–1.25 apfu) and OH (0.72–1.11 apfu) and negligible Cl contents.

4.2.2. Plagioclase-rich veins

Igneous amphibole in plagioclase-rich veins is pale brown at the core to dark green at rim (Fig. 4). Amphibole is Ti-rich ferro-pargasite and shows a decreasing Mg# from core (0.3–0.4) to rim (0.1–0.2). K is

0.2–0.4 apfu (Table 3, Fig. 5). Outer rims of blue-green amphibole are well developed around igneous amphibole in the plagioclase-rich veins (Fig. 4). The compositions of blue-green amphibole vary from hastingsite to ferro-pargasite ($Mg\# = 0.2$, Table 3), with 0.1–0.2 apfu of K (Fig. 5). Remarkably, this amphibole contains up to 0.2 apfu of Cl (Table 3) suggesting late-intrusive circulation of chlorine-rich fluids along the plagioclase-rich veins.

Igneous biotite ($Mg\# = 0.3$) is dark brown at core and dark green at rim, and often interstitial between plagioclase grains. Plagioclase (An_{5-10}) exhibits simple or polysynthetic twinning and rare intergrowths with quartz.

4.2.3. Thermobarometry

Crystallization temperature and pressure are consistent in the three

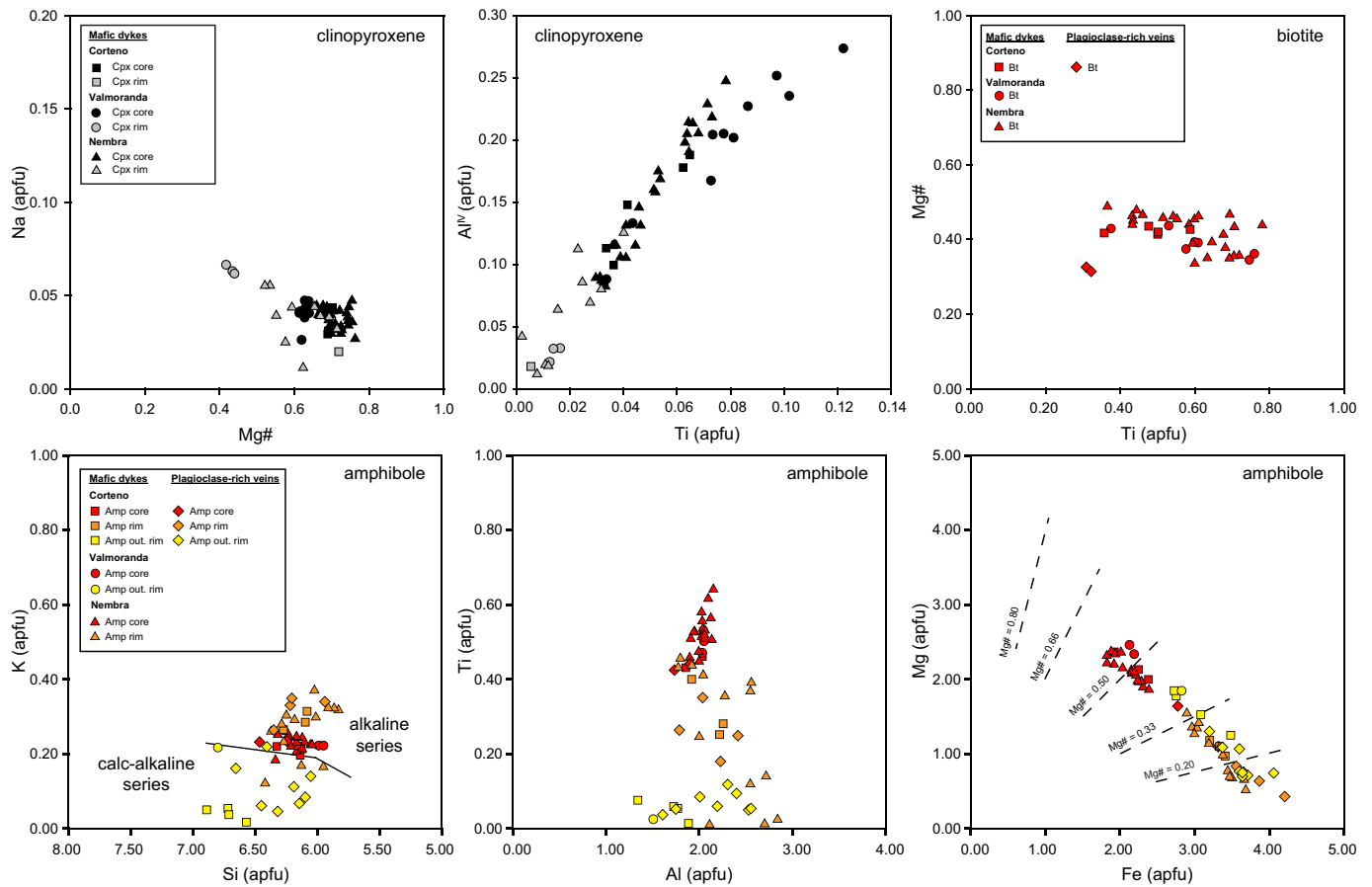


Fig. 5. Composition of magmatic amphibole, biotite, and clinopyroxene in the Edolo diabase dykes. Element concentrations are in apfu. Alkaline and calc-alkaline fields for amphibole classification are from [Ridolfi and Renzulli \(2012\)](#).

localities. Clinopyroxene cores crystallized at 1130 ± 45 °C for a pressure comprised between 0.1 and 0.6 GPa, which are compatible with a shallow depth crystallization. Conversely, amphibole cores crystallized at a markedly lower temperature both in the lamprophyres (960 ± 30 °C) and plagioclase-rich veins (900 ± 30 °C). Amphibole rims retain the lowest crystallization temperature down to 870 ± 30 °C. A temperature of 730 ± 30 °C is determined for the amphibole outer rims, which formed at near-solidus conditions. Lastly, crystallization temperature for igneous biotite was estimated at 860 ± 65 °C in the mafic dykes and 790 ± 65 °C in the plagioclase-rich veins.

4.3. Trace elements composition of igneous minerals

4.3.1. Clinopyroxene

Clinopyroxene cores were analyzed in Nembra, Corteno, and Valmoranda (Fig. 1), where they exhibit significant variations based on locality. In Nembra, clinopyroxene is characterized by relatively high Cr (950–1450 ppm) and moderately high Ni (63–69 ppm) contents. The concentrations of incompatible elements are low, with Zr ranging from 38 to 50 ppm, Hf at 2 ppm, and Y from 17 to 21 ppm. Notably, the contents of Nb (0.1–0.3 ppm) and Ta (<0.1 ppm) are markedly low, with sub-chondritic Nb/Ta ratios.

In Corteno, clinopyroxene is characterized by relatively low Cr (12–153 ppm) and Ni (34–56 ppm) contents and moderate concentrations of incompatible elements (Zr = 40–91 ppm, Hf = 2–4 ppm, Y = 29–39 ppm). Nb and Ta contents are in the range of 0.1–0.5 ppm and <0.1 ppm, respectively, with sub-chondritic Nb/Ta ratios.

In Valmoranda, clinopyroxene is characterized by very low Cr (8–13

ppm) and Ni (10–14 ppm) contents. Conversely, the concentrations of Zr, Hf, and Y are relatively high, with Zr ranging from 143 to 160 ppm, Hf from 6 to 7 ppm, and Y from 41 to 51 ppm. Nb (1.2–2.0 ppm) and Ta (0.3–0.4 ppm) contents are higher in comparison with the other localities, but with similar sub-chondritic Nb/Ta ratios.

In the chondrite-normalized incompatible trace element diagram (Fig. 6), clinopyroxene cores show almost chondritic values for Th, U, Nb, and Ta, with a negative anomaly in Sr, which is less pronounced in Nembra compared to Corteno and Valmoranda. In these latter localities, clinopyroxenes also display slightly higher overall concentrations of incompatible trace elements. Consistently, the clinopyroxene in Nembra exhibits lower overall REE contents compared to Corteno and Valmoranda. In the chondrite-normalized REE diagram (Fig. 6), the REE profiles are characterized by similar $(La/Sm)_N$ at 0.3–0.4. On the contrary, $(Gd/Yb)_N$ is higher in Nembra (2.7–3.0), than Corteno (2.1–2.4), and Valmoranda (2.4–2.8). Finally, clinopyroxene from Nembra exhibits a weak to absent Eu anomaly ($Eu/Eu^* = 0.9$ –1.0), while clinopyroxene from the other localities displays a more consistent Eu anomaly ($Eu/Eu^* = 0.8$ –0.9).

4.3.2. Amphibole

Amphibole cores and rims were analyzed in the mafic dykes from Nembra. The cores are characterized by relatively high Ni (24–31 ppm), Ba (80–262 ppm) and Sr (134–211 ppm) contents, with low Zr (456–569 ppm), Hf (15–23 ppm), and Y (112–146 ppm). Cr is up to 17 ppm. Remarkably, amphibole cores show high Nb (215.3–285.0 ppm) and Ta (8.3–11.0 ppm) contents, with super-chondritic Nb/Ta ratios (25–29). Conversely, the amphibole rims show higher Zr (1064–1497

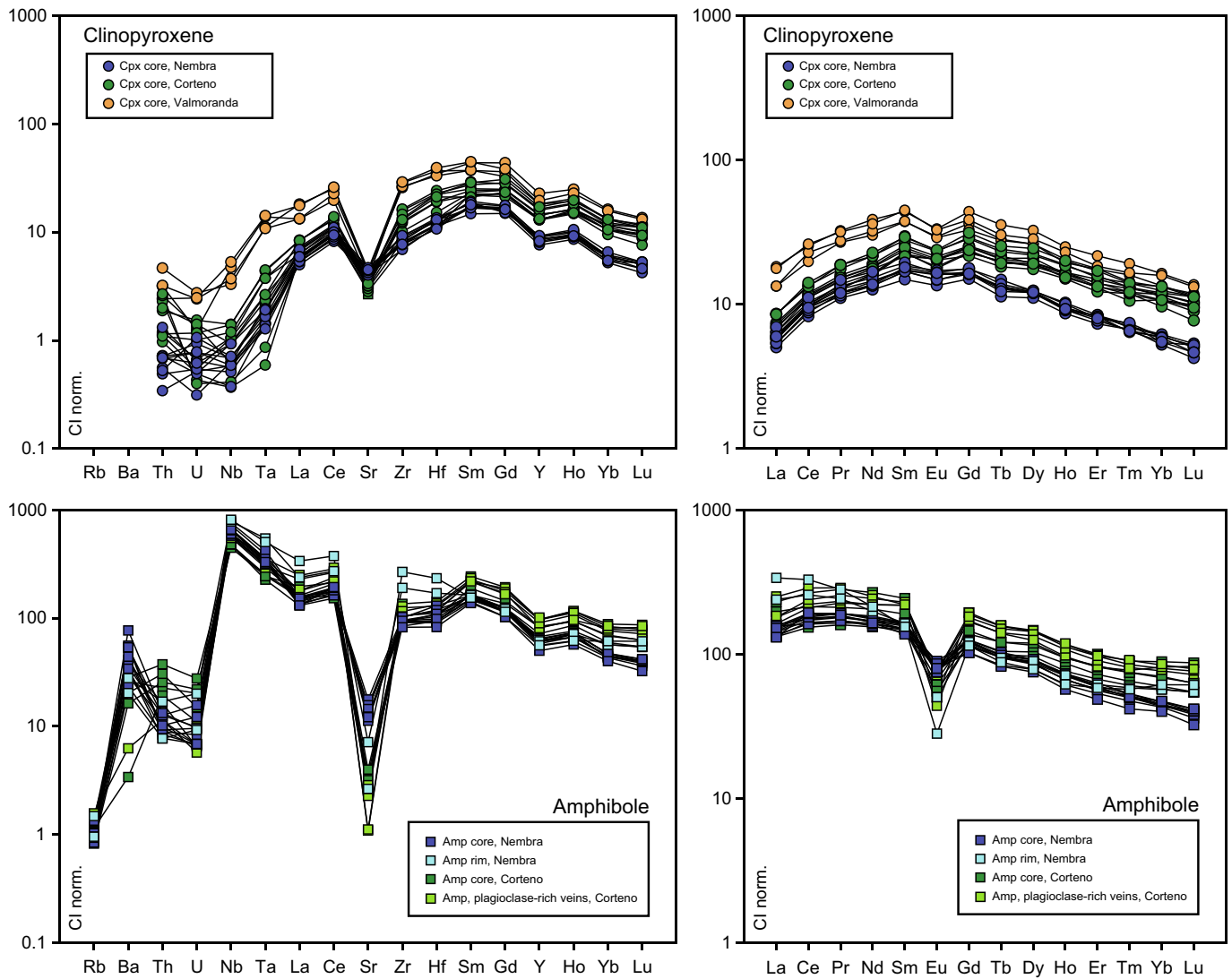


Fig. 6. Chondrite-normalized incompatible element and REE diagrams for igneous clinopyroxene and amphibole. The CI values are from Taylor and McLennan (2009).

ppm) and Hf (31–42 ppm) than the cores, comparable to slightly lower Ni (26–29 ppm) and Y (127–139 ppm), and lower Ba (81–96 ppm) and Sr (32–86 ppm). High Nb (296–307 ppm) and Ta (13–14 ppm) contents in amphibole rims result in super-chondritic Nb/Ta ratios (21–23).

In Corteno, amphibole cores were analyzed in the mafic dykes and plagioclase-rich veins. In mafic dykes, the concentration of Ni in the amphibole cores ranges from 4 to 6 ppm, Ba from 17 to 97 ppm, and Sr from 13 to 97 ppm, which are relatively low. The Cr content is negligible. In contrast, Zr (469–751 ppm), Hf (17–25 ppm), and Y (152–220 ppm) are notably high. Remarkably, there are high Nb (167.7–223.5 ppm) and Ta (5.9–7.8 ppm) contents that result in super-chondritic Nb/Ta ratios (26–30). In the plagioclase-rich veins, amphibole cores exhibit high contents of Zr (577–689 ppm) and Y (182–217 ppm), moderately high Ni (14–28 ppm), and low Cr (2–5 ppm), Ba (21–120 ppm) and Sr (13–35 ppm).

The chondrite-normalized incompatible trace element diagram (Fig. 6) reveals significant positive Nb anomalies in amphibole cores from both Nembra and Corteno. Notably, the amphibole cores from Nembra exhibit considerably lower Th, U, and Sr when compared to those from Corteno. In addition, the chondrite normalized REE patterns (Fig. 6) show lower overall REE contents in Nembra. The REE profiles demonstrate similar $(La/Sm)_N$ ratios, ranging from 0.8 to 1.0, in both localities. However, there is a noticeable difference in HREE

fractionation, with Nembra displaying higher $(Gd/Yb)_N$ ratios from 2.4 to 2.8, whereas Corteno shows ratios from 2.0 to 2.2. All the amphibole core profiles exhibit Eu anomalies, but the anomaly is significantly more pronounced in Corteno ($Eu/Eu^* = 0.2–0.4$) than in Nembra ($Eu/Eu^* = 0.6–0.7$).

In the chondrite-normalized incompatible trace element diagram (Fig. 6), amphibole rims in Nembra exhibit the highest Nb, Ta, Zr, and Hf, but also the lowest Sr contents. These values are associated with a significant negative anomaly in Eu ($Eu/Eu^* = 0.2–0.4$), a relative enrichment in LREE, and the lowest $(Gd/Yb)_N$ ratios of 1.9–2.1 in the REE profiles, similarly to the patterns observed in the amphibole cores in Corteno and plagioclase-rich veins (Fig. 6).

4.3.3. Biotite and ilmenite

Igneous biotite and ilmenite were analyzed in mafic dykes from Nembra and both minerals are characterized by high Nb and Ta contents. Specifically, Nb ranges from 93.6 to 96.4 ppm in biotite, while Ta varies from 3.2 to 3.3 ppm. In ilmenite, Nb is in the range of 176.6 to 356.0 ppm, and Ta in the range of 13.0 to 15.4 ppm. The Nb/Ta ratios are super-chondritic in biotite (26) and from chondritic to super-chondritic in ilmenite (14–26).

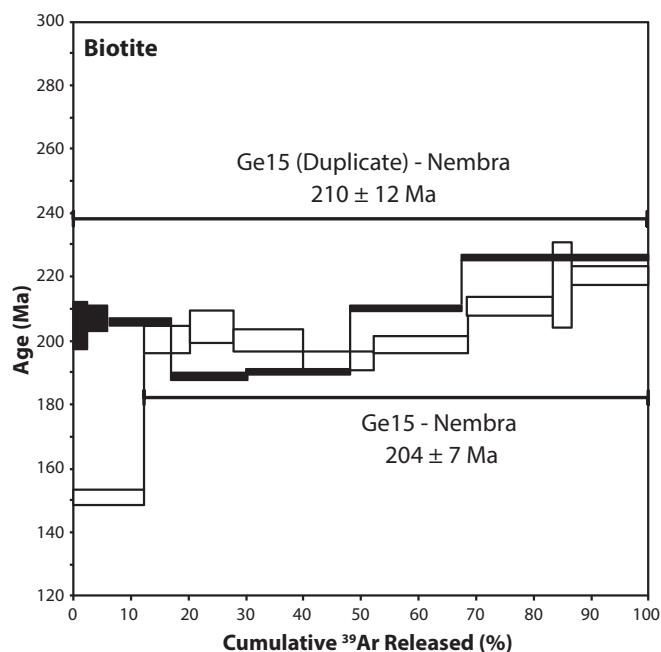


Fig. 7. $^{40}\text{Ar}/^{39}\text{Ar}$ age spectra as a function of ^{39}Ar released. The error boxes of each step are at the 2σ level. The error of ages is given at the 2σ level.

4.4. $^{40}\text{Ar} / ^{39}\text{Ar}$ geochronology

A single igneous biotite grain from Nembra (sample Ge15) yielded a weighted age of 204 ± 7 Ma, which corresponds to 87.5% of ^{39}Ar released and to 8 steps (Fig. 7). The inverse isochron for the plateau steps provides an age at 229 ± 14 Ma. A duplicate of biotite grain yielded a weighted age of 210 ± 12 Ma, which corresponds to 99.5% of ^{39}Ar released and to 7 steps (Fig. 7). The inverse isochron for the plateau steps provides an age at 243 ± 18 Ma. Both ages are concordant in the error bar. However, the incremental heating experiments yielded disturbed spectrum ages and the integrated age must be taken cautiously. The biotite grains analyzed provided saddle-shaped $^{40}\text{Ar}/^{39}\text{Ar}$ ages spectra, which are generally ascribed to an argon excess (Harrison and McDougall, 1981; Lanphere and Dalrymple, 1976). The low-temperature and high-temperature steps yield higher apparent $^{40}\text{Ar}/^{39}\text{Ar}$ ages than the middle-temperature steps. Therefore, the mean-temperature steps in the middle of the spectrum would correspond to a maximum estimate of the age of the grain analyzed (Schaen et al., 2021). In this case we consider the biotite crystallization earlier than 190–200 Ma.

5. Discussion

5.1. Evidence of disequilibrium between igneous minerals

The clinopyroxene grains exhibit highly irregular grain boundaries and are locally rimmed by magmatic amphibole and biotite (Fig. 4). This suggests that clinopyroxene was partially dissolved in the melt from which amphibole and biotite crystallized. In terms of composition, the lack of equilibrium between clinopyroxene and amphibole is confirmed by the higher Mg# of clinopyroxene cores (0.7–0.8) in comparison to that of amphibole (0.4–0.6) and by the exceptionally high Amp/Cpx D^{REE} ratio, which, under equilibrium conditions, should be close to unity (e.g. Tiepolo et al., 2000a). Moreover, the disequilibrium textures and compositions are consistent with the different crystallization temperature estimated for igneous clinopyroxene (1130 ± 45 °C), amphibole (960 ± 30 °C), and biotite (860 ± 65 °C).

5.2. Insights on the composition of the clinopyroxene parental melt

In Nembra, clinopyroxene displays the highest concentrations of compatible elements such as Cr and Ni, along with the lowest overall concentrations of incompatible elements (Fig. 6). These characteristics suggest that mafic dykes from Nembra crystallized from a more primitive melt compared to those from other localities (Fig. 6). Furthermore, the clinopyroxene exhibits the highest Sr content and a weak to absent Eu anomaly since it crystallized, in most cases, before plagioclase. However, it is important to note that the clinopyroxene Mg# at 0.7 to 0.8 is not sufficient to rule out the possibility that a minor degree of differentiation may have characterized the early evolution of this melt.

The composition of the clinopyroxene parental melt was determined in Nembra using solid/liquid partition coefficients ($S^{\text{L/D}}$) that are suitable for the composition and crystallization temperature of the studied rocks (Adam and Green, 2003). As a result, the chondrite-normalized incompatible element concentrations in the clinopyroxene parental melt are overall lower than in the WR compositions (Fig. 8). Notably, the profiles reveal low concentrations of Nb and Ta, with chondritic to slightly super-chondritic Nb/Ta ratios (15–27).

5.3. Insights on the composition of the amphibole parental melt

The igneous amphibole cores crystallized from an evolved melt, as indicated by Mg# between 0.4 and 0.6. Furthermore, the amphibole compositions display depletion in Rb and Sr, along with a negative Eu anomaly in the REE profiles (Fig. 6). These observations indicate that amphibole crystallization occurred concurrently with biotite and plagioclase, as evidenced by microstructural analysis.

The amphibole cores in Nembra crystallized from a less evolved melt when compared to those in Corteno. The amphibole in Nembra is indeed richer in Cr and Ni and generally shows depletion in incompatible elements. Furthermore, it exhibits less pronounced Sr and Eu anomalies and more fractionated HREEs than in Corteno. The similarity between the amphibole rims in Nembra and amphibole cores in Corteno confirms that, in the latter locality, amphibole crystallized from a more evolved melt.

The composition of the amphibole parental melt was determined in

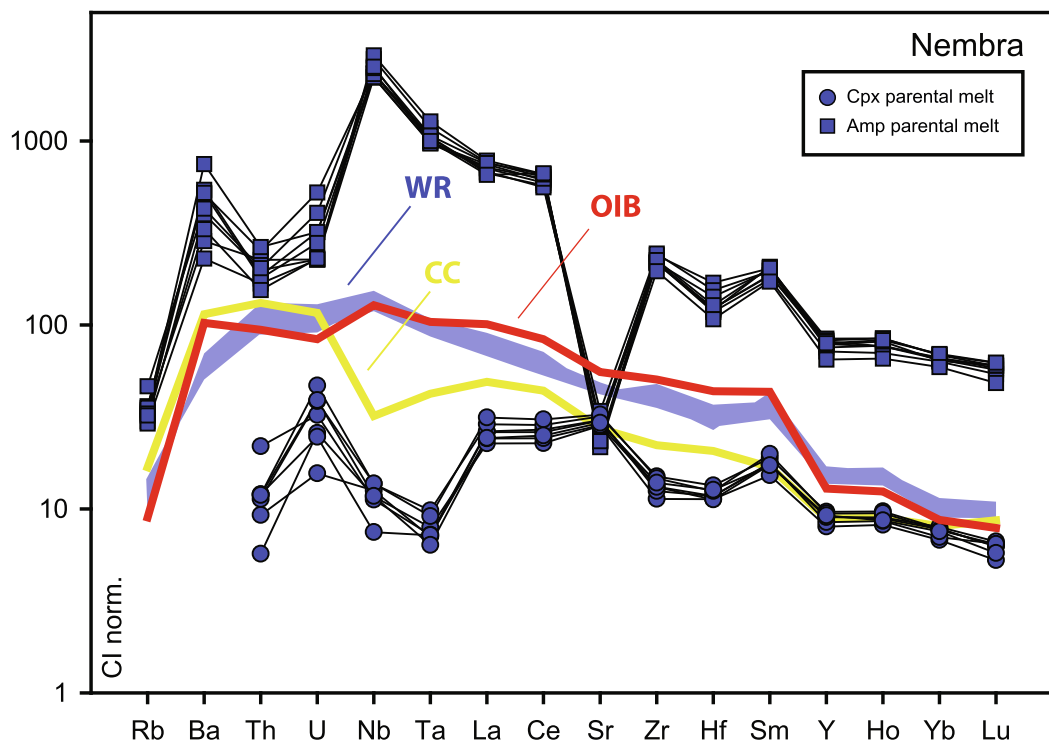


Fig. 8. Chondrite-normalized incompatible element diagram for the parental melts of clinopyroxene and amphibole in Nembra. The CI values are from [Taylor and McLennan \(2009\)](#). WR (whole rock) compositions of the Edolo diabase dykes from Nembra are included for comparison. The reference values for OIB (ocean island basalt) are from [Sun and McDonough \(1989\)](#), for CC (continental crust) are from [Rudnick and Fountain \(1995\)](#).

Nembra using partition coefficients from [Adam and Green \(2003\)](#). Remarkably, the amphibole parental melt is characterized by significantly high concentrations of Nb (828–1096 ppm), Ta (25–33 ppm), and LREE, with markedly super-chondritic Nb/Ta ratios (32–37).

5.4. Genetic relationships between parental melts

A genetic connection between the parental melts of clinopyroxene and amphibole is investigated as both these minerals coexist in the same dykes. To test this hypothesis, the evolution from clinopyroxene to amphibole parental melts was modeled through fractional crystallization. The effectiveness of clinopyroxene fractionation in the evolution of the Edolo diabase dykes is supported by the correlation between MgO and Cr ([Fig. 3](#)). In addition, weak Eu anomalies in the composition of some clinopyroxene grains may suggest minor fractionation of plagioclase ([Fig. 6](#)). Fractionation of Ti-rich phases is unlikely due to the overall high Ti contents in WR compositions and in most of the minerals that crystallized at different temperatures.

As a result, achieving LREE concentrations similar to those in the amphibole parental melt through fractional crystallization is improbable, unless extremely low residual melt fractions are taken into account. Furthermore, even with extreme fractional crystallization of clinopyroxene and plagioclase, it was not possible to achieve enrichment in Nb and Ta, as seen in the amphibole parental melt. Hence, the distinction between the parental melts of amphibole and clinopyroxene is unlikely to be solely due to fractional crystallization.

It is worth noting that a higher concentration of Nb in amphibole compared to clinopyroxene is common in mafic systems. For example, [Coogan et al. \(2001\)](#) showed that intercumulus amphibole can exhibit Nb concentrations 100–1000 times greater than those of early formed cumulus clinopyroxene in a Mid-Atlantic Ridge gabbro. However, this intercumulus amphibole is fluorine-rich and crystallized in interstitial spaces from a highly evolved melt at a temperature near the solidus ($T = 860 \pm 30$ °C). Instead, this study focuses on the cores of Ti-rich amphiboles that are mostly subhedral and crystallized at 960 ± 30 °C under

markedly supersolidus conditions.

It is known that the D_{Nb} , D_{Ta} , and $D_{Nb/Ta}$ ratios for dehydrogenated amphibole can vary by order of magnitude, mostly depending on the content of Fe, Mg, and Ti in the melt [Tiepolo et al. \(2000b\)](#). Nevertheless, high concentrations of Nb and Ta and high Nb/Ta ratios are also observed in biotite and ilmenite that crystallized concurrently with amphibole in the Edolo diabase dykes. For this reason, the compositional gap between clinopyroxene and amphibole parental melts is unlikely to be explained by a not appropriate choice of the S/LD values. Instead, the high Nb and Ta contents and ratios reflect the composition of the melt from which amphibole, biotite, and ilmenite crystallized.

The compositional difference between the clinopyroxene and amphibole parental melts can be attributed to crustal assimilation. In this view, assimilation likely occurred after clinopyroxene but before amphibole crystallization. Crustal assimilation can account for the increased concentrations of LREEs in the amphibole parental melt. However, it is challenging to achieve high Nb and Ta contents and ratios by assimilating conventional crustal rocks with low Nb and Ta contents and subchondritic ratios ([Rudnick and Fountain, 1995](#)). Therefore, if crustal assimilation is considered, the distinctive compositions of assimilated rocks are crucial in shaping the composition of the amphibole parental melt.

Alternatively, clinopyroxene and amphibole may have crystallized from magmas with contrasting compositions. The formation of these magmas might have occurred either concomitantly due to heterogeneities in the source rocks, fluids, and evolutionary pathways, or diachronously. In the latter case, clinopyroxene could have crystallized from a less differentiated melt with low Nb and Ta contents and was subsequently assimilated by a second, more evolved, Nb- and Ta-rich alkaline melt. Despite the differences between these hypotheses, rocks with high Nb and Ta contents and ratios are considered here as potential sources for the amphibole parental melt.

5.5. Geodynamic implications

The compositional difference between clinopyroxene and amphibole parental melts could lead to contrasting interpretations in terms of tectonic environment. The relatively primitive composition of the clinopyroxene parental melt resembles what is expected in arc settings (e.g. Foley et al., 2002). Unfortunately, the crystal chemical filter does not permit clinopyroxene to incorporate LIL elements that could serve as a proxy for a more effective tectonic interpretation. Contrastingly, the amphibole seems to have crystallized from an alkaline melt (Figs. 5 and 8), a feature reflected by the WR compositions of the Edolo diabase dykes (Fig. 3) and commonly associated with continental rifting (e.g., Galli et al., 2019).

In the Triassic framework of the Adria passive margin, the high-K shoshonitic Predazzo complex in the eastern Southalpine domain is the nearest intrusive complex to the Edolo diabase dykes. This complex is of middle Triassic age and exhibits arc affinity (Casetta et al., 2018a; Sloman, 1989) broadly comparable to that of the clinopyroxene parental melt. Middle Triassic igneous and volcanoclastic rocks with arc affinity are also found in the southeasternmost Southalpine domain, Dinarides (Storck et al., 2019; Lustrino et al., 2019 and ref. therein), and the eastern Austroalpine domain (Eisenkappel / Karawanken, Miller et al., 2011 and ref. therein). Conversely, in the western Southalpine domain, middle Triassic diorites in the outer gabbro of Finero display a more transitional character with a MORB imprint, suggesting a back-arc setting. A possible link to a subduction zone is here highlighted by the high-H₂O content of these rocks (Zanetti et al., 2013). Transitional to tholeiitic igneous products are also found in the extensive extrusive and subvolcanic rocks within the middle Triassic sedimentary sequences of the central Southalpine domain, along with minor intermediate dykes (Cassinis et al., 2008; Lustrino et al., 2019). In this framework, the parental melt of clinopyroxene in the Edolo diabase dykes shares more similarities with the rocks of the eastern Southalpine domain.

Previous authors have often suggested a genetic link between middle Triassic magmatism and Paleotethys subduction to the east. However, establishing a direct link between these processes is challenging, primarily due to the inferred distance between the Southalpine domain and this subduction zone (Edel et al., 2018; Van Hinsbergen et al., 2020). On the contrary, the disputed arc affinity observed in the Middle Triassic magmatism of the central to eastern Southalpine domain is more recently interpreted as a consequence of the melting of the sub-continental mantle, along with Variscan to Permian igneous cumulates (Storck et al., 2019 and ref. therein). This process would have involved amphibole-peritectic melting acting as a water source, while Ti, Nb, and Ta being retained in restitic rutile and ilmenite. A second given hypothesis to explain the arc affinity of middle Triassic magmatism is the reactivation after about 100 million years of the metasomatized mantle wedge of the Variscan subduction, whose features were not fully erased by the Permian magmatism (Beltrán-Triviño et al., 2016; De Min et al., 2020; Lustrino et al., 2019; Sloman, 1989). Regardless of the chosen scenario, both hypotheses require an uprising thermal state in the sub-continental mantle after the Permian event, which aligns well with the Permian-Triassic asthenospheric upwelling.

On the other hand, the amphibole parental melt in the Edolo diabases exhibits a high-Nb alkaline signature. In the late Triassic, alkaline to carbonatitic magmatism affected the western and eastern Southalpine domain (Casetta et al., 2019; Galli et al., 2019; Zaccarini et al., 2004). Some of these rocks exhibit moderate to high Nb contents (Cassinis et al., 2008; Galli et al., 2019; Schaltegger et al., 2015; Stähle et al., 2001), or, at least, an absence of Ti, Nb, and Ta negative anomalies (Casetta et al., 2019), characteristics that were present in the middle Triassic magmatism. The high concentrations of Ti, Nb, and Ta in the Edolo diabase dykes may be tentatively explained by melting of Nb- and Ta-rich sources during progressive asthenosphere upwelling, similarly to what has been suggested in the western Southalpine domain, where the late Triassic alkaline magmatism is interpreted as due to melting of

amphibole-rich mantle domains (Galli et al., 2019).

The late Triassic alkaline to carbonatitic magmatism anticipated the opening of the Alpine Tethys of some 25–35 Myr (cfr. Rebay et al., 2018; Gleißner et al., 2021; Nicollet et al., 2022 and references therein). To the west, the coeval emplacement of mafic complexes and alkaline lamprophyres of the CAMP announces the opening of the Atlantic Ocean (Najih et al., 2019). A correlation between these magmatic provinces has been suggested by similar ages and geochemical characters (Denyszyn et al., 2018 and ref. therein), as well as by paleogeographic reconstructions that show the Alpine Tethys as a branch of the Atlantic Ocean (Doré and Stewart, 2002; Van Hinsbergen et al., 2020).

6. Conclusions

In the central Southalpine domain, the Ti-rich alkaline Edolo diabase dykes were emplaced at the end of the Triassic in the Variscan basement. The early-crystallized clinopyroxene shows low Nb and Ta contents and ratios, and contrasts with the compositions of late-crystallized amphibole, biotite, and ilmenite. Such compositional evolution is likely not solely due to fractional crystallization. The clinopyroxene parental melt may reflect the composition of the sub-continental mantle inherited from Variscan subduction or transformed during the Permian, as proposed in the eastern part of the Southalpine domain for explaining the disputed arc affinity of the middle Triassic magmatism (e.g., Lustrino et al., 2019; Storck et al., 2019). On the other hand, the amphibole composition is likely influenced by successive melting or assimilation of Nb-Ta-rich phases, a process similar to that which explains the composition of the late Triassic magmatism in the western Southalpine domain (Galli et al., 2019). The composition of the Triassic Edolo diabase dykes is thus influenced by the heterogeneity of the Adriatic lithosphere that underwent continuous asthenospheric upwelling due to Permian-Triassic extensional tectonics.

Author statement

All listed authors have contributed to the development and execution of this research. No undisclosed authors have contributed to this work. This research was conducted with the highest ethical standards, adhering to the guidelines and regulations governing scientific research.

Declaration of Competing Interest

The authors declare that there are no conflicts of interest that could affect the impartiality of the research.

Acknowledgments

This work is part of the PhD thesis of M. Filippi. G. Sessa and A. Risplendente are acknowledged for technical assistance. The authors express their gratitude to F. Casetta and an anonymous reviewer for their constructive reviews, which have greatly contributed to enhancing the quality of the text. A special thanks is also extended to G. Shellnutt for his meticulous editorial handling. This work received support from the Italian Ministry for University and Research (MUR) through the project “Dipartimenti di Eccellenza 2023-27”.

Appendix A. Supplementary data

Supplementary data to this article can be found online at <https://doi.org/10.1016/j.lithos.2023.107435>.

References

- Adam, J., Green, T., 2003. The influence of pressure, mineral composition and water on trace element partitioning between clinopyroxene, amphibole and basaltic melts. *Eur. J. Mineral.* 15 (5), 831–841.

- Beltrán-Triviño, A., Winkler, W., von Quadt, A., Gallhofer, D., 2016. Triassic magmatism on the transition from Variscan to Alpine cycles: evidence from U–Pb, Hf, and geochemistry of detrital minerals. *Swiss J. Geosci.* 109 (3), 309–328.
- Berra, F., Carminati, E., 2010. Subsidence history from a backstripping analysis of the Permo-Mesozoic succession of the Central Southern Alps (Northern Italy). *Basin Res.* 22 (6), 952–975.
- Berra, F., Tiepolo, M., Caironi, V., Siletto, G.B., 2015. U–Pb zircon geochronology of volcanic deposits from the Permian basin of the Orobic Alps (Southern Alps, Lombardy): chronostratigraphic and geological implications. *Geol. Mag.* 152, 429–443.
- Bertotti, G., Siletto, G.B., Spalla, M.I., 1993. Deformation and metamorphism associated with crustal rifting: the Permian to Liassic evolution of the Lake Lugano-Lake Como area (Southern Alps). *Tectonophysics* 226 (1–4), 271–284.
- Carminati, E., Siletto, G.B., Battaglia, D., 1997. Thrust kinematics and internal deformation in basement-involved fold and thrust belts: the eastern Orobic Alps case (Central Southern Alps, northern Italy). *Tectonics* 16 (2), 259–271.
- Casetta, F., Coltorti, M., Ickert, R.B., Bonadiman, C., Giacomoni, P.P., Ntafos, T., 2018a. Intrusion of shoshonitic magmas at shallow crustal depth: T–P path, H₂O estimates, and AFC modeling of the Middle Triassic Predazzo Intrusive Complex (Southern Alps, Italy). *Contrib. Mineral. Petrol.* 173 (7), 57.
- Casetta, F., Coltorti, M., Marrocchino, E., 2018b. Petrological evolution of the Middle Triassic Predazzo intrusive complex, Italian Alps. *Int. Geol. Rev.* 60 (8), 977–997.
- Casetta, F., Ickert, R.B., Mark, D.F., Bonadiman, C., Giacomoni, P.P., Ntafos, T., Coltorti, M., 2019. The alkaline lamprophyres of the Dolomitic Area (Southern Alps, Italy): markers of the late Triassic change from orogenic-like to anorogenic magmatism. *J. Petrol.* 60 (6), 1263–1298.
- Cassinis, G., Cortesogno, L., Gaggero, L., Perotti, C.R., Buzzi, L., 2008. Permian to Triassic geodynamic and magmatic evolution of the Bresciana Prealps (eastern Lombardy, Italy). *Boll. Soc. Geol. Ital.* 127 (3), 501–518.
- Coogan, L.A., Wilson, R.N., Gillis, K.M., MacLeod, C.J., 2001. Near-solidus evolution of oceanic gabbros: insights from amphibole geochemistry. *Geochim. Cosmochim. Acta* 65 (23), 4339–4357.
- De Graciansky, P.C., Roberts, D.G., Tricart, P., 2011. The Western Alps, from Rift to Passive Margin to Orogenic Belt: An Integrated Geoscience Overview. Elsevier, Amsterdam, The Netherlands, p. 397.
- De Min, A., Velicogna, M., Ziberna, L., Chiaradia, M., Alberti, A., Marzoli, A., 2020. Triassic magmatism in the European Southern Alps as an early phase of Pangea break-up. *Geol. Mag.* 1–23.
- Denyszyn, S.W., Fiorentini, M.L., Maas, R., Dering, G., 2018. A bigger tent for CAMP. *Geology* 46 (9), 823–826.
- di Paola, S., Spalla, M.I., 2000. Contrasting tectonic records in pre-Alpine metabasites of the Southern Alps (Lake Como, Italy). *J. Geodyn.* 30 (1–2), 167–189.
- di Paola, S., Spalla, M.I., Gosso, G., 2001. New structural mapping and metamorphic evolution of the Domaso Cortafo Zone (Southern Alps—Lake Como). *Memorie di Scienze Geologiche*, Padova 53, 1–14.
- Diella, V., Spalla, M.I., Tunesi, A., 1992. Contrasting thermomechanical evolutions in the Southalpine metamorphic basement of the Orobic Alps (central Alps, Italy). *J. Metamorph. Geol.* 10 (2), 203–219.
- Doré, A.G., Stewart, I.C., 2002. Similarities and differences in the tectonics of two passive margins: the Northeast Atlantic Margin and the Australian North West Shelf. In: Keep, M., Moss, S.J. (Eds.), *The Sedimentary Basins of Western Australia*, 3. Petroleum Exploration Society of Australia (PESA), pp. 89–117.
- Edel, J.B., Schulmann, K., Lexa, O., Lardeaux, J.M., 2018. Late Palaeozoic palaeomagnetic and tectonic constraints for amalgamation of Pangea supercontinent in the European Variscan belt. *Earth Sci. Rev.* 177, 589–612.
- Filippi, M., Spalla, M.I., Pigazzini, N., Diella, V., Lardeaux, J.-M., Zanoni, D., 2021. Cld-St-and-bearing assemblages in the central Southalpine Basement: markers of an evolving thermal regime during Variscan convergence. *Minerals* 11 (10), 1124.
- Filippi, M., Zanoni, D., Rebay, G., Roda, M., Regorda, A., Lardeaux, J.-M., Spalla, M.I., 2022. Quantification of Alpine metamorphism in the Edolo diabase, Central Southern Alps. *Geosciences* 12 (8), 312.
- Foley, S., Tiepolo, M., Vannucci, R., 2002. Growth of early continental crust controlled by melting of amphibolite in subduction zones. *Nature* 417 (6891), 837–840.
- Galli, A., Grassi, D., Sartori, G., Gianola, O., Burg, J.P., Schmidt, M.W., 2019. Jurassic carbonatite and alkaline magmatism in the Ivrea zone (European Alps) related to the breakup of Pangea. *Geology* 47 (3), 199–202.
- Gleißner, P., Franz, G., Frei, D., 2021. Contemporaneous opening of the Alpine Tethys in the Eastern and Western Alps: constraints from a late Jurassic gabbro intrusion age in the Glockner Nappe, Tauern Window, Austria. *Int. J. Earth Sci.* 110, 2705–2724.
- Gosso, G., Siletto, G.B., Spalla, M.I., 1997. International ophiolite symposium field excursion guide—continental rifting to ocean floor metamorphism (21st–23rd September 1995): first day: HT/LP metamorphism and structures in the South-Alpine basement near Lake Como, Orobic Alps; intracontinental imprints of the Permo-Triassic rifting. *Ophioliti* 22, 133–145.
- Gosso, G., Spalla, M.I., Bini, A., Siletto, G.B., Berra, F., Forcella, F., 2012. Note Illustrative della Carta Geologica d'Italia alla scala 1: 50.000, Foglio 057 Malonno. ISPRA and Regione Lombardia.
- Guergouz, C., Martin, L., Vanderhaeghe, O., Thébaud, N., Fiorentini, M., 2018. Zircon and monazite petrochronologic record of prolonged amphibolite to granulite facies metamorphism in the Ivrea-Verbanò and Strona-Ceneri zones, NW Italy. *Lithos* 308, 1–18.
- Harrison, T.M., McDougall, I., 1981. Excess ⁴⁰Ar in metamorphic rocks from Broken Hill, New South Wales: implications for ⁴⁰Ar/³⁹Ar age spectra and the thermal history of the region. *Earth Planet. Sci. Lett.* 55 (1), 123–149.
- Jourdan, F., Renne, P.R., 2007. Age calibration of the Fish Canyon sanidine 40Ar/39Ar dating standard using primary K–Ar standards. *Geochim. Cosmochim. Acta* 71 (2), 387–402.
- Ketcham, R.A., 2015. Technical note: calculation of stoichiometry from EMP data for apatite and other phases with mixing on monovalent anion sites. *Am. Mineral.* 100, 1620–1623.
- Klötzli, U.S., Sinigoi, S., Quick, J.E., Demarchi, G., Tassinari, C.C., Sato, K., Günes, Z., 2014. Duration of igneous activity in the Sesia magmatic system and implications for high-temperature metamorphism in the Ivrea–Verbanò deep crust. *Lithos* 206, 19–33.
- Koppers, A.A., 2002. ArArCALC—software for 40Ar/39Ar age calculations. *Comput. Geosci.* 28 (5), 605–619.
- Lanphere, M.A., Dalrymple, G.B., 1976. Identification of excess ⁴⁰Ar by the ⁴⁰Ar/³⁹Ar age spectrum technique. *Earth Planet. Sci. Lett.* 32 (2), 141–148.
- Lardeaux, J.-M., Spalla, M.I., 1991. From granulites to eclogites in the Sesia zone (Italian Western Alps): a record of the opening and closure of the Piedmont Ocean. *J. Metamorph. Geol.* 9 (1), 35–59.
- Li, X., Zhang, C., 2022. Machine learning thermobarometry for biotite-bearing magmas. *J. Geophys. Res.* Solid Earth 127 (9) e2022JB024137.
- Locock, A.J., 2014. An Excel spreadsheet to classify chemical analyses of amphiboles following the IMA 2012 recommendations. *Comput. Geosci.* 62, 1–11.
- Lustrino, M., Abbas, H., Agostini, S., Caggiati, M., Carminati, E., Gianolla, P., 2019. Origin of Triassic magmatism of the Southern Alps (Italy): constraints from geochemistry and Sr–Nd–Pb isotopic ratios. *Gondwana Res.* 75, 218–238.
- Manzotti, P., Rubatto, D., Zucali, M., El Korh, A., Cenki-Tok, B., Ballèvre, M., Engi, M., 2018. Permian magmatism and metamorphism in the Dent Blanche nappe: constraints from field observations and geochronology. *Swiss J. Geosci.* 111 (1–2), 79–97.
- Marotta, A.M., Roda, M., Conte, K., Spalla, M.I., 2018. Thermo-mechanical numerical model of the transition from continental rifting to oceanic spreading: the case study of the Alpine Tethys. *Geol. Mag.* 155 (2), 250–279.
- Miller, C., Thöni, M., Goessler, W., Tessadri, R., 2011. Origin and age of the Eisenkappel gabbro to granite suite (Carinthia, SE Austrian Alps). *Lithos* 125 (1–2), 434–448.
- Najih, A., Montero, P., Verati, C., Chabou, M.C., Fekkak, A., Baïdier, L., Ezzouhairi, H., Bea, F., Michard, A., 2019. Initial Pangean rifting north of the West African Craton: insights from late Permian U–Pb and 40Ar/39Ar dating of alkaline magmatism from the Eastern Anti-Atlas (Morocco). *J. Geodyn.* 132, 101670.
- Nicollet, C., Paquette, J.-L., Bruand, E., Bosse, V., Pereira, I., 2022. Crystallisation and fast cooling of the (meta)gabbro from the Chenaillet ophiolite (Western Alps): in-situ U–Pb dating of zircon, titanite, monazite and xenotime in textural context. *Lithos* 414, 106620.
- Peressini, G., Quick, J.E., Sinigoi, S., Hofmann, A.W., Fanning, M., 2007. Duration of a large mafic intrusion and heat transfer in the lower crust: a SHRIMP U–Pb zircon study in the Ivrea–Verbanò Zone (Western Alps, Italy). *J. Petrol.* 48 (6), 1185–1218.
- Putirka, K.D., 2008. Thermometers and barometers for volcanic systems. *Rev. Mineral. Geochem.* 69 (1), 61–120.
- Putirka, K., 2016. Amphibole thermometers and barometers for igneous systems and some implications for eruption mechanisms of felsic magmas at arc volcanoes. *Am. Mineral.* 101 (4), 841–858.
- Quick, J.E., Sinigoi, S., Peressini, G., Demarchi, G., Wooden, J.L., Sbisà, A., 2009. Magmatic plumbing of a large Permian caldera exposed to a depth of 25 km. *Geology* 37 (7), 603–606.
- Real, C., Fassmer, K., Carosi, R., Froitzheim, N., Rubatto, D., Groppo, C., Munker, C., Ferrando, S., 2023. Carboniferous-Triassic tectonic and thermal evolution of the middle crust section of the Dervio-Olgiasca Zone (Southern Alps). *J. Metamorph. Geol.* 41 (5), 685–718.
- Rebay, G., Spalla, M.I., 2001. Emplacement at granulite facies conditions of the Sesia–Lanzo metagabbros: an early record of Permian rifting? *Lithos* 58 (3–4), 85–104.
- Rebay, G., Maroni, M., Siletto, G.B., Spalla, M.I., 2015. Superposed syn-metamorphic structures of the Alpine and pre-Alpine convergent cycles in the Southalpine basement of the Orobic Alps (Northern Italy). *J. Maps* 11 (1), 168–180.
- Rebay, G., Zanoni, D., Langone, A., Luoni, P., Tiepolo, M., Spalla, M.I., 2018. Dating of ultramafic rocks from the Western Alps ophiolites discloses late Cretaceous subduction ages in the Zermatt-Saas Zone. *Geol. Mag.* 155, 298–315.
- Ridolfi, F., Renzulli, A., 2012. Calcic amphiboles in calc-alkaline and alkaline magmas: thermobarometric and chemometric empirical equations valid up to 1,130° C and 2.2 GPa. *Contrib. Mineral. Petrol.* 163 (5), 877–895.
- Roda, M., Regorda, A., Spalla, M.I., Marotta, A.M., 2019. What drives Alpine Tethys opening? Clues from the review of geological data and model predictions. *Geol. J.* 54 (4), 2646–2664.
- Roda, M., Spalla, M.I., Filippi, M., Lardeaux, J.-M., Rebay, G., Regorda, A., Zanoni, D., Zucali, M., Gosso, G., 2023. Metamorphic remnants of the Variscan orogeny across the Alps and their tectonic significance. *Geosciences* 13 (10), 300.
- Rudnick, R.L., Fountain, D.M., 1995. Nature and composition of the continental crust: a lower crustal perspective. *Rev. Geophys.* 33 (3), 267–309.
- Sassi, R., Mazzoli, C., Merle, R., Brombin, V., Chiaradia, M., Dunkley, D.J., Marzoli, A., 2020. HT-LP crustal syntectonic anatexis as a source of the Permian magmatism in the Eastern Southern Alps: evidence from xenoliths in the Euganean trachytes (NE Italy). *J. Geol. Soc. Lond.* 177 (6), 1211–1230.
- Schaen, A.J., Jicha, B.R., Hodges, K.V., Vermeesch, P., Stelten, M.E., Mercer, C.M., et al., 2021. Interpreting and reporting 40Ar/39Ar geochronologic data. *Bulletin* 133 (3–4), 461–487.
- Schaltegger, U., Brack, P., 2007. Crustal-scale magmatic systems during intracontinental strike-slip tectonics: U, Pb and Hf isotopic constraints from Permian magmatic rocks of the Southern Alps. *Int. J. Earth Sci.* 96 (6), 1131–1151.

- Schaltegger, U., Ulianov, A., Müntener, O., Ovtcharova, M., Peytcheva, I., Vonlanthen, P., Antognini, M., Giralda, F., 2015. Megacrystic zircon with planar fractures in miaskite-type nepheline pegmatites formed at high pressures in the lower crust (Ivrea Zone, southern Alps, Switzerland). *Am. Mineral.* 100 (1), 83–94.
- Schiavinato, G., 1954. Sulle rocce diabasiche comprese negli Scisti di Edolo in Val Camonica (Lombardia). *Rendiconti della Società Mineralogica Italiana* 11, 233–261.
- Schuster, R., Stüwe, K., 2008. Permian metamorphic event in the Alps. *Geology* 36 (8), 603–606.
- Sloman, L.E., 1989. Triassic shoshonites from the dolomites, northern Italy: alkaline arc rocks in a strike-slip setting. *J. Geophys. Res. Solid Earth* 94 (B4), 4655–4666.
- Smye, A.J., Lavier, L.L., Zack, T., Stockli, D.F., 2019. Episodic heating of continental lower crust during extension: a thermal modeling investigation of the Ivrea-Verbano Zone. *Earth Planet. Sci. Lett.* 521, 158–168.
- Spalla, M.I., Carminati, E., Ceriani, S., Oliva, A., Battaglia, D., 1999. Influence of deformation partitioning and metamorphic re-equilibration on P–T path reconstruction in the pre-Alpine basement of central Southern Alps (Northern Italy). *J. Metamorph. Geol.* 17, 319–336.
- Spalla, M.I., Siletto, G.B., di Paola, S., Gosso, G., 2000. The role of structural and metamorphic memory in the distinction of tectono-metamorphic units: the basement of the Como lake in the Southern Alps. *J. Geodyn.* 30 (1–2), 191–204.
- Spalla, M.I., Zanoni, D., Gosso, G., Zucali, M., 2009. Deciphering the geologic memory of a Permian conglomerate of the Southern Alps by pebble P–T estimates. *Int. J. Earth Sci.* 98 (1), 203–226.
- Spalla, M.I., Zanoni, D., Marotta, A.M., Rebay, G., Roda, M., Zucali, M., Gosso, G., 2014. The transition from Variscan collision to continental break-up in the Alps: insights from the comparison between natural data and numerical model predictions. *Geol. Soc. Lond. Spec. Publ.* 405 (1), 363–400.
- Stähle, V., Frenzel, G., Hess, J.C., Saupé, F., Schmidt, S.T., Schneider, W., 2001. Permian metabasalt and Triassic alkaline dykes in the northern Ivrea zone: clues to the post-Variscan geodynamic evolution of the Southern Alps. *Schweiz. Mineral. Petrogr. Mitt.* 81 (1), 1–21.
- Storck, J.C., Brack, P., Wotzlav, J.F., Ulmer, P., 2019. Timing and evolution of Middle Triassic magmatism in the Southern Alps (northern Italy). *J. Geol. Soc. Lond.* 176 (2), 253–268.
- Sun, S.S., McDonough, W.F., 1989. Chemical and isotopic systematics of oceanic basalts: implications for mantle composition and processes. *Geol. Soc. Lond. Spec. Publ.* 42 (1), 313–345.
- Taylor, S.R., McLennan, S., 2009. *Planetary Crusts: Their Composition, Origin and Evolution*, vol. 10. Cambridge University Press.
- Tiepolo, M., Vannucci, R., Bottazzi, P., Oberti, R., Zanetti, A., Foley, S., 2000a. Partitioning of rare earth elements, Y, Th, U, and Pb between pargasite, kaersutite, and basanite to trachyte melts: implications for percolated and veined mantle. *Geochem. Geophys. Geosyst.* 1 (8).
- Tiepolo, M., Vannucci, R., Oberti, R., Foley, S., Bottazzi, P., Zanetti, A., 2000b. Nb and Ta incorporation and fractionation in titanian pargasite and kaersutite: crystal–chemical constraints and implications for natural systems. *Earth Planet. Sci. Lett.* 176 (2), 185–201.
- Tribuzio, R., Thirlwall, M.F., Messiga, B., 1999. Petrology, mineral and isotope geochemistry of the Sondalo gabbroic complex (central Alps, Northern Italy): implications for the origin of post-Variscan magmatism. *Contrib. Mineral. Petrol.* 136 (1–2), 48–62.
- Van Acherbergh, E., Ryan, C.G., Jackson, S.E., Griffin, W.L., 2001. Data reduction software for LA-ICP-MS: appendix. In: Sylvester, P.J. (Ed.), *Laser Ablation-ICP Mass Spectrometry in the Earth Sciences: Principles and Applications*, pp. 239–243.
- Van Hinsbergen, D.J., Torsvik, T.H., Schmid, S.M., Mañenco, L.C., Maffione, M., Vissers, R.L., Gürer, D., Spakman, W., 2020. Orogenic architecture of the Mediterranean region and kinematic reconstruction of its tectonic evolution since the Triassic. *Gondwana Res.* 81, 79–229.
- Zaccarini, F., Stumpfl, E.F., Garuti, G., 2004. Zirconolite and Zr–Th–U minerals in chromitites of the Finero complex, Western Alps, Italy: evidence for carbonatite-type metasomatism in a subcontinental mantle plume. *Can. Mineral.* 42 (6), 1825–1845.
- Zanchi, A., Zanchetta, S., Berio, L., Berra, F., Felletti, F., 2019. Low-angle normal faults record early Permian extensional tectonics in the Orobic Basin (Southern Alps, N Italy). *Ital. J. Geosci.* 138 (2), 184–201.
- Zanetti, A., Mazzucchelli, M., Sinigoi, S., Giovanardi, T., Peressini, G., Fanning, M., 2013. SHRIMP U–Pb zircon Triassic intrusion age of the Finero mafic complex (Ivrea-Verbano Zone, Western Alps) and its geodynamic implications. *J. Petrol.* 54 (11), 2235–2265.
- Zanoni, D., Spalla, M.I., 2018. The Variscan evolution in basement cobbles of the Permian Ponteranica formation by microstructural and petrologic analysis. *Ital. J. Geosci.* 137 (2), 188–207.
- Zanoni, D., Spalla, M.I., Gosso, G., 2010. Vestiges of lost tectonic units in conglomerate pebbles? A test in Permian sequences of the Southalpine Orobic Alps. *Geol. Mag.* 147 (1), 98–122.